High-Throughput, High-Resolution Echelle Deep-UV Raman Spectrometer

Sergei V. Bykov,[a] Bhavya Sharma,[b] Sanford A. Asher[a,*]

[a] *Department of Chemistry, University of Pittsburgh, Pittsburgh, PA 15260, USA*
[b] *Department of Chemistry, Northwestern University, Evanston, IL 60208, USA*

We constructed an ultrahigh-throughput, high-resolution ultraviolet (UV) Raman spectrograph that utilizes a high-efficiency filter-stage monochromator and a high-dispersion Echelle spectrograph. The spectrograph utilizes a total of six mirrors and two gratings, with an overall efficiency at 229 nm of ~18%. The limiting resolution of our spectrometer is 0.6 cm^{-1} full width half-maximum (FWHM), as measured for 229 nm Rayleigh scattering. Use of a 1 mm–wide entrance slit gives rise to an approximately 10 cm^{-1} FWHM resolution at 229 nm. The ultrahigh spectrograph throughput enables ultrahigh signal-to-noise ratio, deep UV Raman spectra that allow us to monitor <1% changes in peptide bond composition. The throughput is measured to be 35-fold greater than conventional deep UV Raman spectrometers.

Index Headings: **UV Raman spectrometer; Echelle; High-throughput; High-resolution; Biomolecules; Peptide; Protein.**

INTRODUCTION

Ultraviolet (UV) resonance Raman spectroscopy is a highly informative technique for investigating the structure and dynamics of biological macromolecules and other complex systems.[1–7] The resonance Raman spectra are sensitive to very small changes in molecular bond lengths and bond angles, because these small changes significantly impact the ground-state vibrational frequencies as well as the coupling of vibrations to the resonant electronic transition(s). Time-dependent measurements can be used to follow reactions such as protein folding down into picosecond and nanosecond time intervals.[8–15] The resonance Raman spectra can have high spatial selectivity, because the excitation can be chosen to be resonant with particular absorption bands localized in specific regions of interest in the macromolecule.

UV resonance Raman spectra are generally signal-to-noise (S/N) limited due to the low excitation powers that can be used. High excitation powers can result in thermal or photochemical damage to samples. Furthermore, the higher peak powers of low-duty cycle lasers can result in nonlinear optical phenomena that complicate the measured spectra and confound spectral interpretations.

Low-UV-resonance Raman spectral S/N also results from the generally low throughputs of existing deep UV Raman spectrometers. To improve UV Raman S/N, we have built a revolutionary high-throughput, high-dispersion, high-resolution UV Raman spectrograph that dramatically increases the spectral S/N and the information content of measured deep UV Raman spectra. We increased the spectrometer throughput by increasing the spectrometer dispersion; this allows us to open the spectrometer entrance slit.

Our spectrometer utilizes a 1 mm slit width that gives a spectral resolution bandwidth of ~10 cm^{-1}, appropriate for 229 nm UV Raman spectra of condensed-phase samples. This bandwidth is comparable to the homogeneous line widths of Raman bands of biological macromolecules.[16] The resulting high spectrometer throughput allows us to use short, 10 min spectral accumulation times to easily monitor small protein secondary-structure conformational changes that involve less than 1% of the protein peptide bonds. Thus, this spectrometer allows us to monitor conformational changes of a single peptide bond for a protein of 100 amino acids.

SPECTROMETER DESIGN

Figure 1 shows the optical diagram of the Echelle spectrograph we constructed. The spectrograph utilizes two gratings; one regular grating is used in the filter stage, while the other, an Echelle grating, is used in the high-dispersion spectrograph stage. Raman and Rayleigh scattered light is focused on the entrance slit S_1 that is tilted by an angle ξ_1 about the optic axis *X* to compensate for the vertical tilt of the image due to the out-of-plane positioning of the diffraction gratings. The filter stage spectrograph optic axis lies in the *XY* plane, which contains the centers of entrance slit S_1, mirrors M_1, M_2, and M_3, and grating G_1. Grating G_1 is displaced by $\Delta X = -7.5$ cm from S_1, while M_2 is displaced by $\Delta X = -7.5$ cm from M_1. The distance between S_1 and M_1 is approximately 126 cm.

The light is collimated by M_1 and directed to the holographic grating G_1 (1200 grooves/mm, purchased from Richardson Gratings, Inc.). The dispersed, collimated light is collected and focused by mirror M_2 and directed to the flat turning mirror M_3 (all mirrors are UV enhanced, Al coated with MgF_2) that focuses the light to slit S_2 and transfers the diverging light to turning mirror M_4 in the Echelle-based stage of the spectrometer. We define the Echelle spectrograph-stage plane of diffraction as the *XZ* plane perpendicular to the Echelle grating grooves. We define the spectrograph plane *XY* as the vertical plane perpendicular to the plane of diffraction *XZ* that is horizontal. The middle slit S_2 located between M_3 and M_4 blocks the Rayleigh scattered light and selects the spectral region of interest (approximately 10 nm) to be dispersed by the Echelle grating. The middle slit is tilted by an angle $\xi_2 = \xi_1 + \Delta\xi$, where ξ_1 is a tilt of the entrance slit S_1, and $\Delta\xi$ is the additional tilt required by the out-of-plane configuration of grating G_1. Mirrors M_1 and M_2 are not vertically above one other, but M_2 is displaced by $\Delta X = 7.5$ cm to allow more space between grating G_1 and turning mirror M_3.

Plane mirror M_4 directs the diverging beam to collimating mirror M_5. The collimated beam is sent to the Echelle grating

Received 12 December 2012; accepted 28 March 2013
* Author to whom correspondence should be sent. E-mail: asher@pitt.edu.
DOI: 10.1366/12-06960

0003-7028/13/6708-0873/0

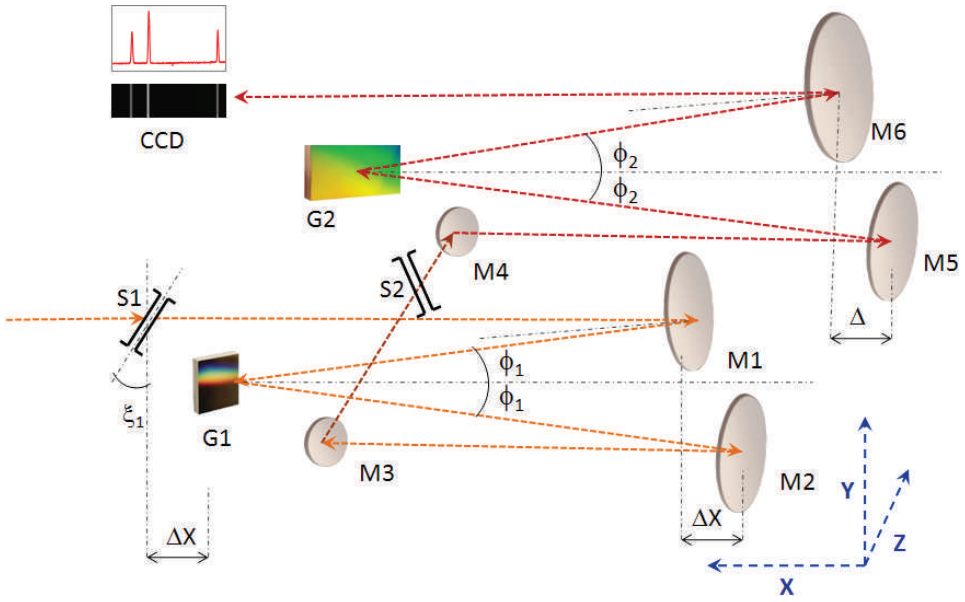

FIG. 1. Diagram of high-resolution, high-throughput spectrograph. *X* is parallel to the spectrometer optical axis; the *XY* plane is orthogonal to the spectrograph dispersion plane *XZ*. S_1 is the entrance slit that is tilted by angle $\xi_1 = 23°$about *X* to compensate for the tilt introduced by the out-of-plane diffraction gratings G_1 and G_2. M_1, M_2, M_5, and M_6 are off-axis parabolic mirrors. The on-axis focal lengths are $f_{M_1} = f_{M_2} = f_{M_3} = 126.37$ cm (49.75 in), $f_{M_4} = 133.68$ cm (52.63 in) and zonal radii are $ZR_{M_1} = ZR_{M_2} = ZR_{M_3} = 11.43$ cm (4.5 in), $Z_{M_4} = 19.05$ cm (7.5 in). G_1 is the filter-stage low stray light, 1200 grooves/mm blazed holographic grating, while G_2 is a high-dispersion Echelle grating, 316 grooves/mm, blazed at 63°. The middle slit S_2 separates the filter and Echelle spectrograph stages. M_3 and M_4 are plane turning mirrors. ϕ_1 is the angle of the incident and diffracted light relative to *X* about G_1. ϕ_2 is the angle between the incident and diffracted light about *X* about the Echelle grating G_2 of the dispersing spectrograph. Centers of the slit S_1, grating G_1, mirrors M_1, M_2, and M_3 are in the same vertical plane *XY*. Centers of the CCD, grating G_2, mirrors M_4, M_5, and M6 are in the same vertical plane, the $X'Y'$ main-dispersion spectrograph plane.

G_2 to be dispersed and directed to mirror M_6, which focuses the dispersed light onto the charge-coupled device (CCD) detector. The out-of-plane angles of the filter spectrometer stage and Echelle spectrograph stages are $\phi_1 \approx \phi_2 \approx 6°$.These out-of-plane angles are in the *XY* plane and occur between the incident and *X* and the diffracted beam and *X* (Fig. 1).

Choice of Dispersing Gratings. Echelle gratings have very high dispersion and resolving power. High-quality Echelle gratings demonstrate high reflectivity over a broad spectral range, with only a weak dependence of reflectivity on the polarization of the incident light. Echelle gratings have low groove densities (usually between 23 to 316 grooves/mm) and are blazed for operation at high orders at high-diffraction angles (usually between 32 and 79°). After careful review and multiple tests of commercially available Echelle gratings from different manufacturers, we chose a 316 grooves/mm, 63° blazed, MgF_2-protected, Al-coated Echelle grating manufactured by Richardson Gratings, Inc. This grating shows good reflectivity in the UV region >190 nm, very little polarization dependence of reflectivity (Fig. 2), and is commercially available in large sizes. Similar Echelle gratings from other manufacturers showed lower efficiency. We found that the manufacturer quoted efficiency and the actual efficiencies we measured often dramatically differed.

The angular dispersion of a diffraction grating at wavelength λ is determined by the incidence (α) and diffraction (β) angles. If the Echelle grating is operated in the Littrow configuration where $\alpha = \beta = \theta$ (Fig. 3) the angular dispersion, D_a is

$$D_a = \frac{2 \tan \theta}{\lambda} \tag{1}$$

Theoretically, an infinite dispersion can be obtained if θ approaches 90°. In practice, the use of high values of θ is limited due to the increasingly stronger contributions of groove defects on dispersion and resolution, and the increasing contribution of ghost aberration due to high blaze angles, as well as the decreased effective width of the grating at high θ.

We concluded that use of our Echelle grating that is blazed at $\theta = 63°$ provides a close to optimal dispersion and resolution for a grating of reasonable width. This grating also enables a wide enough free spectral range (FSR) and high resolving power, R_{pw} , for the Littrow case $\alpha = \beta = \theta$:

$$R_{pw} = \frac{2W \sin \theta}{\lambda} \tag{2}$$

For the 63° blazed perfect Echelle with a ruled width, $W =$ 206 mm at 229 nm in the Littrow configuration, the resolving power is calculated to be $R_{pw} = 1.6 \times 10^6$. The effective experimental resolving power can be less due to irregularity in grating groove periodicity and surface optical defects. The resolution of the spectrometer is determined by the spectrograph entrance and exit slit widths (or the CCD detector pixel widths), as well as spectrograph optical aberrations.

One of the disadvantages of low groove-density gratings such as the Echelle is their resulting limited free spectral range:

$$\mathrm{FSR} = \frac{\lambda_c}{n} \tag{3}$$

where *n* is the diffraction order, and λ_c is central wavelength.

If our 63° blazed, 316 grooves/mm Echelle were used in the Littrow configuration and illuminated with the Stokes Raman spectra excited at 229 nm, the diffracted intensity will be concentrated near the 24th order, with an FSR ~10 nm. To avoid spectral-order overlap, the spectrometer must include a

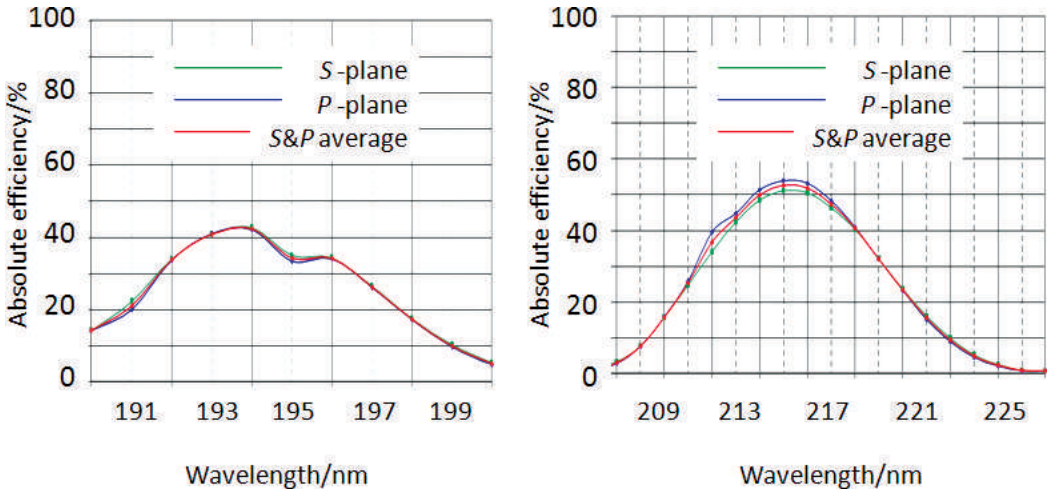

FIG. 2. Efficiency of the 316 grooves/mm, 63° blazed Echelle grating measured for the 29th order for 190–200 nm light and in the 26th order for 207–227 nm light. (Data provided by Richardson Gratings, Inc.)

wavelength-selecting filter stage that selects this approximately 10 nm Raman region of interest.

Echelle Efficiency Dependence on Wavelength and Polarization. Figure 2 shows the measured efficiency of our 316 grooves/mm, 63° blazed Echelle for the 29th and 26th order (data provided by Richardson Gratings, Inc.).The reflectivity for the *s*- and *p*-polarized light differs by only by a few percent in the UV region. The reflectivity of the Echelle grating varies from approximately 60 (in the visible) to 40% in the UV at 193 nm and ~53% at 216 nm.

CHOICE OF ECHELLE OPTICAL CONFIGURATION

Efficiency Dependence on Optical Configuration. Blazed gratings are most efficient when used in the Littrow configuration when the incident and diffracted beams are normal to the groove surface (incident at the grating blaze angle θ). Figure 3 shows the experimentally measured dependence of the absolute grating efficiency measured for the 11th order at 488 nm (316 grooves/mm Echelle, 63° blazed)

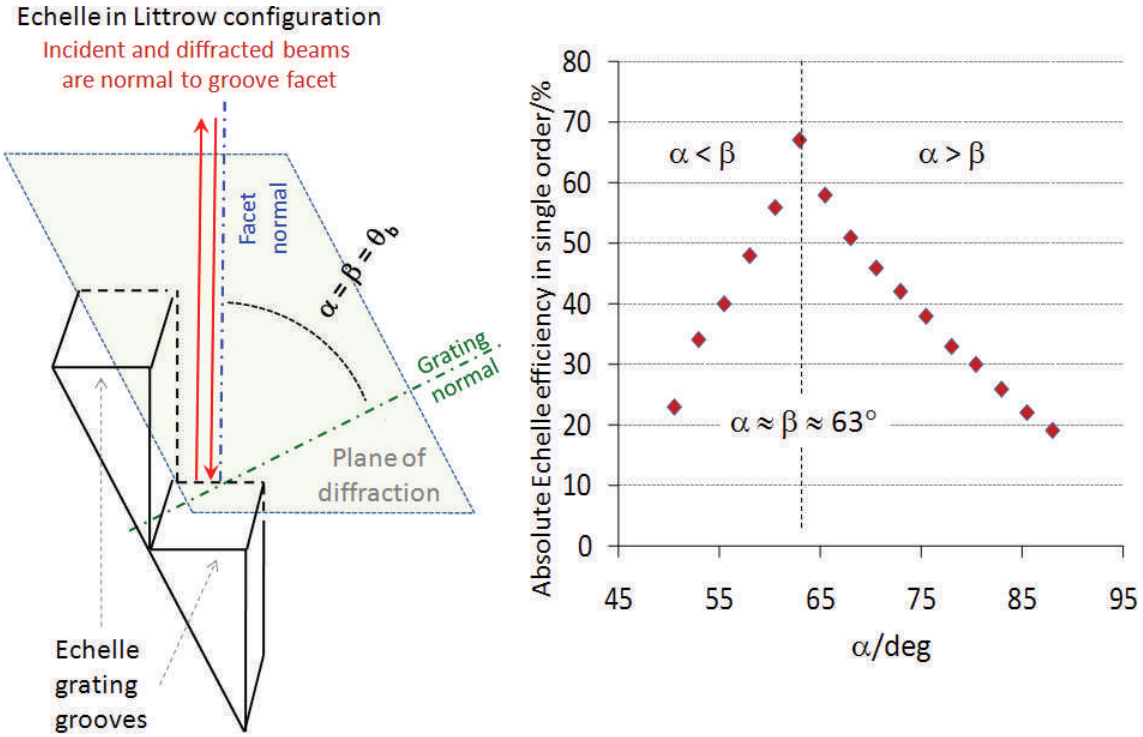

FIG. 3. Echelle grating in Littrow configuration showing two adjacent triangular Echelle grooves and measured dependence of the 316 grooves/mm, 63° blazed Echelle grating efficiency on the angle of incidence, α. Echelle grating was irradiated with 488 nm laser light and the absolute efficiency was measured for the 11th order. The blaze angle, θ_b, is the angle between the grating normal and groove facet normal. The plane of diffraction is perpendicular to the grating grooves.

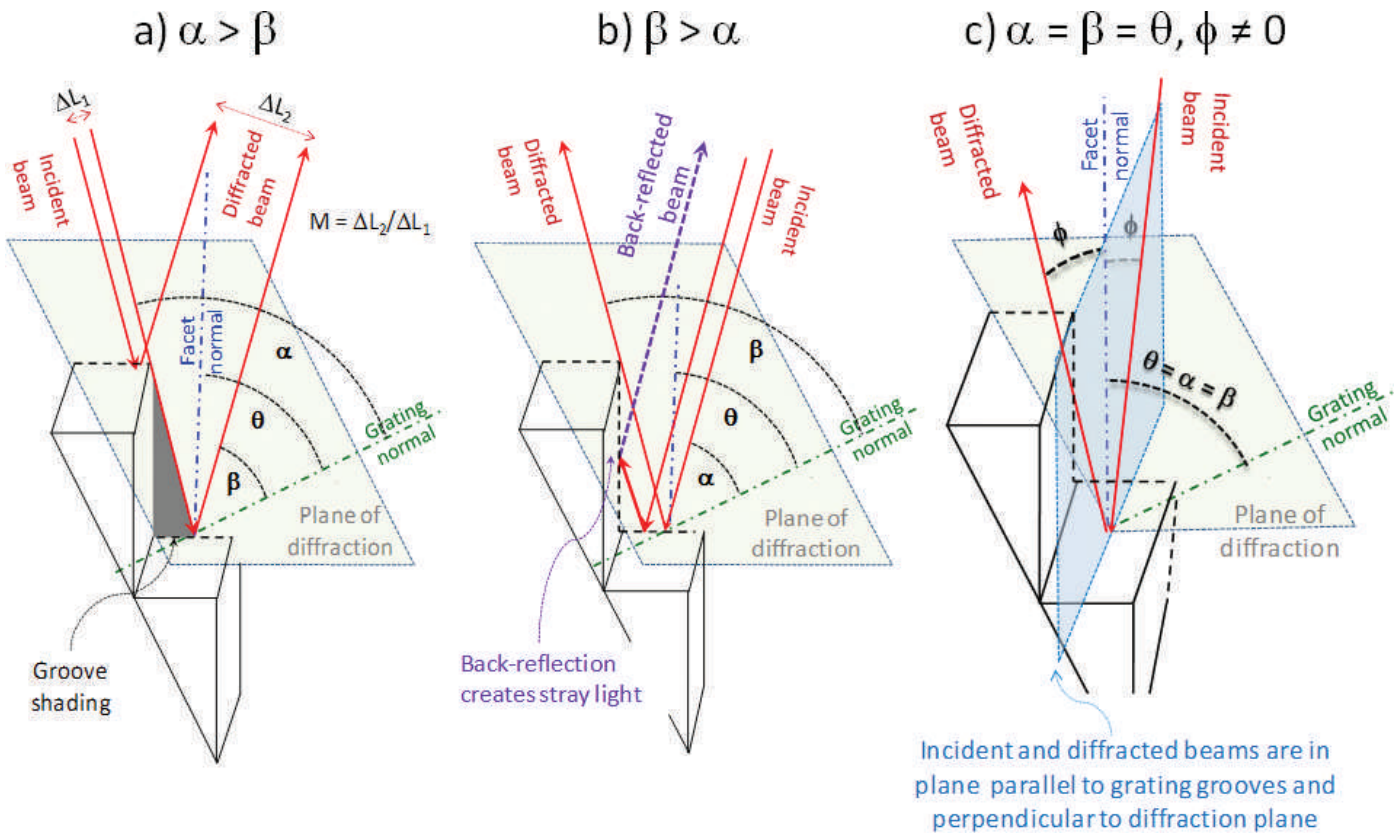

FIG. 4. Possible Echelle grating optical configurations. Echelle grating has right triangular–shaped grooves with narrowed facets to diffract the incident light. In all three cases, the diffracted beam parallels the specularly reflected beam. α = angle of incidence; β = angle of diffraction; ϕ = angle between incident and diffracted beam out of the plane of diffraction. (**A**) Case $\alpha > \beta$ results in groove shading and anamorphic magnification $M = \Delta L_2/\Delta L_1$. (**B**) Case $\beta > \alpha$ results in partial back-reflection of the incident beam from the wide facet of the groove. (**C**) Out-of-plane Littrow configuration $\alpha = \beta = \theta$, $\phi \neq 0$ is least affected by groove shading, anamorphism, or back-reflection. This case causes a tilt of the slit image as discussed in the text.

for different angles of incidence. When $\alpha \approx \beta \approx \theta = 63°$, the grating is in a configuration close to Littrow and shows a maximum efficiency, where approximately 70% of the incident monochromatic light is diffracted into a single order. The grating efficiency decreases with the α angular deviation from 63°, which is equivalent to the angular deviation from the Littrow condition. The Echelle efficiency drops faster for $\alpha < \beta$ case compared with $\alpha > \beta$, probably due to back-reflection light losses (Fig. 4b).

It is impossible to utilize the grating exactly at the Littrow configuration, since the incident and diffracted beams must be separable. We considered three possible optical configurations for the Echelle grating. Two of these are "in-plane" configurations, where the incident and diffracted light both lie in the plane of diffraction. We also considered an "out-of-plane" configuration, where the incident and diffracted beams are tilted by an angle ϕ about the plane of diffraction (Fig. 4).These possibilities include $\alpha > \beta$, $\phi = 0$ (in-plane of diffraction), $\beta > \alpha$, $\phi = 0$ (in-plane of diffraction), and $\alpha = \beta = \theta$, $\phi \neq 0$ (out-of-plane Littrow configuration).

These cases were theoretically and experimentally analyzed by Schroeder and Hilliard.[16] Their analysis showed that in case $\beta > \alpha$, a significant part of the incident light is lost due to reflections from the wide facets of the grooves (Fig. 4b). This results in a decreased grating efficiency and increased stray light. The grating efficiency drops rapidly as the angular deviation from the Littrow configuration increases (Fig. 3). Thus, case $\beta > \alpha$ is not a good choice for a high-throughput spectrometer.

Case $\alpha > \beta$ shows smaller light losses. Thus, this configuration is frequently used in Echelle-based spectrometers.[18,19] Its major drawback is that a significant anamorphic magnification occurs for the diffracted beam. Figure 4a shows two rays incident on a groove of the grating, where the right-hand ray is glancing along the edge of the upper groove facet. The two rays are separated by a ΔL_1. After diffraction the separation between these rays increases to ΔL_2, which results in magnification of the diffracted beam by $M = \Delta L_2/\Delta L_1$. For our 63° Echelle, the diffracted beam will be twice magnified in the plane of diffraction for a deviation from the Littrow configuration of 10°. This will result in a twofold decreased photon flux per detector pixel element. This will necessitate a larger detector in order to monitor the highly dispersed image. Anamorphic magnification also increases the slit image width and spectrograph aberrations.

The Echelle grating has the highest efficiency in the case (c) out-of-plane Littrow configuration, where $\alpha = \beta = \theta$, $\phi \neq 0$. This case does not show grating anamorphism or back-reflection. This configuration, while optimal for a high-throughput, high-dispersion Raman instrument, results in a tilt of the focused image of the originally vertical entrance slit.

Aberrations Introduced by Out-of-Plane Grating Spectrometer. In the out-of-plane configuration, the incident and diffracted beams form an angle ϕ about the plane of diffraction; this results in new aberrations not present for in-

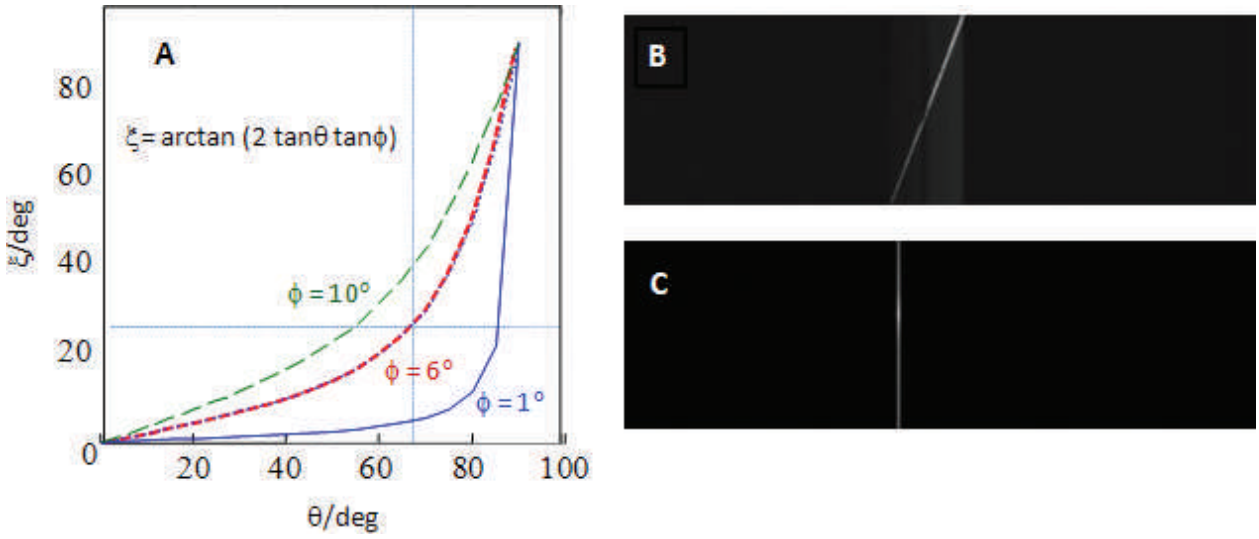

FIG. 5. (**A**) Calculated dependence of the tilt angle, ξ of the slit image on the CCD detector from vertical orientation as a function of grating blaze angle θ for three non-planar angles: $\phi = 10°$, $\phi = 6°$, and $\phi = 1°$. (**B**). Image of the vertical entrance slit on a CCD. (**C**) Image of the entrance slit, which is tilted approximately 23° from the vertical orientation on CCD camera to compensate for aberration caused by the out-of-plane grating illumination.

plane spectrometers.[20] In an out-of-plane spectrometer the spectral lines will be tilted by an angle ξ:[21]

$$\xi = \arctan(2 \tan\theta \tan\phi) \tag{4}$$

The tilt angle ξ rapidly grows as the grating blaze angle θ or out-of-plane angle ϕ increases (Fig. 5A).

For our 63° blazed Echelle and a non-planarity angle of $\phi = 6°$, the image of the slit on the detector will be approximately 23° tilted from the vertical. This tilt would, if uncompensated, significantly affect the measured bandwidth and the spectral resolution. Thus, we tilt the entrance slit by 23° to compensate for this image tilt.

Filter Stage. In order to avoid overlap of spectral lines from neighboring orders, the spectral range of the light dispersed by the Echelle grating must be limited to the FSR of the Echelle grating. For our 63° blazed, 316 grooves/mm Echelle grating, the FSR is approximately 10 nm in the UV. Echelle gratings are also known to have relatively high levels of stray light that could significantly degrade Raman spectral measurements. Thus, the filter stage spectrometer performs two crucial functions—it selects an approximately 10 nm spectral region of interest to be dispersed by the Echelle stage, and it blocks the Rayleigh scattered light that is the main source of stray light in Raman spectrometers. The filter stage utilizes a 1200 grooves/mm, holographic grating blazed for the UV region manufactured by Richardson Gratings, Inc. This diffraction grating has moderate dispersion, high UV efficiency, and low stray light.

The filter-stage spectrometer has a layout similar to that of the Echelle spectrograph stage. We utilize an out-of-diffraction plane angle of ϕ_1 approximately 6° (Fig. 1). This out-of-plane filtering stage will reject the Rayleigh light more effectively, since the out-of-plane design removes the possibility of "multiple dispersion," This multiple dispersion phenomenon is common in in-plane spectrometers.[22] At certain grating orientations light diffracted into the $n - 1$ or $n + 1$ orders (where n is main order) can be returned to the grating by collimating or focusing mirrors and get re-diffracted.[23,24] This multiply dispersed light can significantly contribute to spectrometer stray light, especially in the UV spectral region where diffraction orders becomes more closely spaced. In addition the out-of-plane layout is more compact compared with the in-plane Czerny–Turner design.

Choice of Mirrors. To decrease the aberrations that would result from off-axis illumination of spherical mirrors, we used off-axis parabolic mirrors. For our spectrometer, we utilized 126.37 cm (49.75 inch) focal length, 12.7 cm (5 inch) diameter off-axis parabolic mirrors for M_1, M_2, and M_5 (Fig. 4). Parabolic mirror M_6 is larger, with a diameter of 20.3 cm (8 in) and focal length 133.68 cm (52.63 in), since a bigger aperture is required to collect the dispersed light after the Echelle grating. The longer M_6 focal length allows more space for the CCD detector (Fig. 1).The spectrometer reciprocal linear dispersion, RLD is determined by the angular dispersion of the grating, D_a and the focal length, f_c, of the final spectrograph mirror:

$$\mathrm{RLD} = \frac{1}{D_a f_c} \tag{5}$$

For the deep UV region (λ approximately 210), RLD approximately 0.04 nm/mm or approximately eight times greater than our existing high-resolution Raman spectrometer.[25] These off-axis parabolic mirrors were coated with a UV-enhanced Al protected by MgF_2 and were purchased from Dodgen Optical, L.L.C.

Sample Illumination and Scattered Light–Collecting Optics. High S/N Raman measurements require optimization of the sample illumination and the scattered light collection to transfer as much of the Raman scattered light through the spectrograph entrance slit as possible. The preferred "back-scattering" geometry for absorbing samples (Fig. 6) focuses the laser beam of diameter d onto a sample by using a focusing lens L_1. The beam spot size on the sample is mainly determined by the lens L_1 spherical aberrations and the lens diffraction that depends on the lens type and focal length as well as on the laser beam quality.

The Raman and Rayleigh scattered light is then collected by lens L_2 that collimates the light and directs it to focusing lens

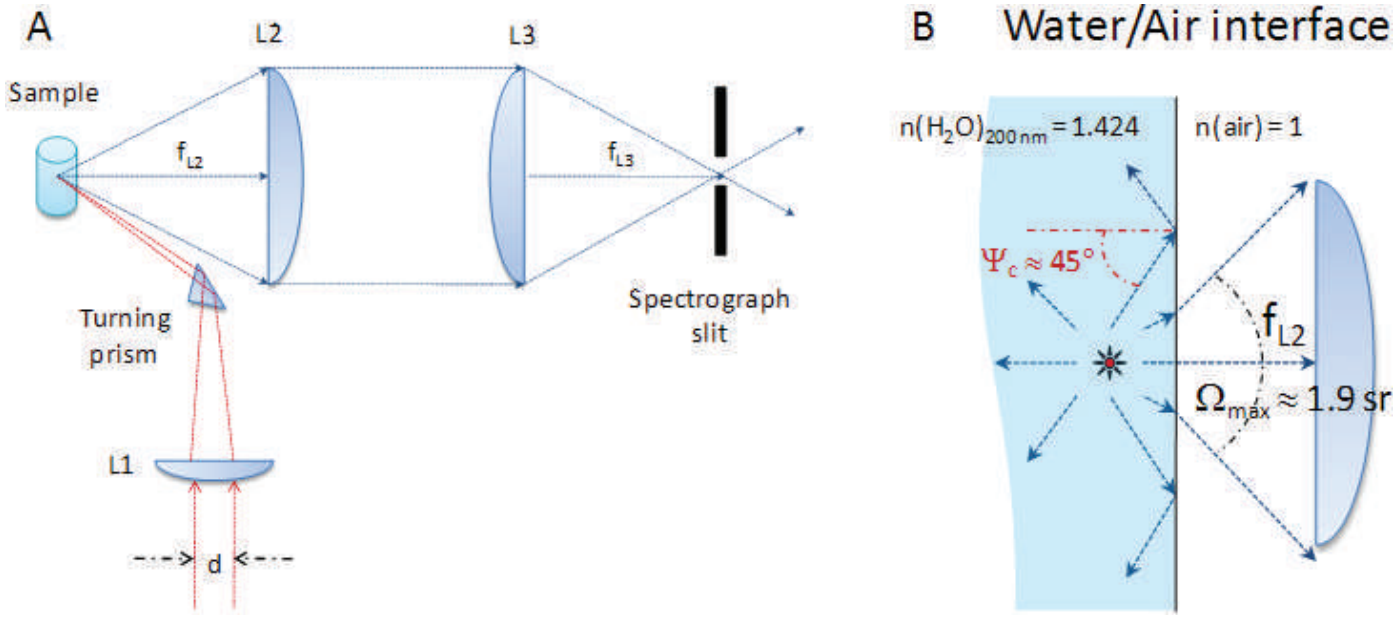

FIG. 6. (**A**) Backscattering sample excitation illumination geometry. L_1 is the laser-light focusing lens, L_2 is the scattered light collecting–collimating lens, L_3 is the scattered light focusing lens. *d* is the incident laser beam diameter. (**B**) For the liquid sample, the maximum solid angle of scattered light that can be collected Ω_{max} is limited by the critical reflection angle Ψ_c. For a water/air interface at 200 nm $\Psi_c \approx 45°$ and $\Omega_{max} \approx 1.9$ sr.

L_3, which focuses the collimated light onto the spectrograph entrance slit. In general, lens L_2 must have as small an *f*-number as possible in order to maximize collection of Raman scattered light. Lens L_3 is should be *f*-number matched to the first spectrometer collimating mirror.

Due to the difference in focal lengths of L_2 and L_3, the spot on the spectrograph entrance slit is that of the sample laser spot size, magnified by a factor equal to the ratio of the focal lengths f_{L_3}/f_{L_2}. If $f_{L_3} \gg f_{L_2}$, the magnification is large, and a significant part of the collected Raman scattered light could be blocked by the entrance slit. Finally, the focusing of lens L_3 could be subject to significant spherical aberrations, because the incident collimated scattered light beam diameter *d* is large and equal to the lens diameter.

The best shape for a spherical lens that produces minimal aberrations depends on the illumination geometry and on refractive index of the lens, which depends on wavelength. For on-axis illumination, plano-convex lenses have close to minimum transverse and longitudinal spherical aberrations if the convex side faces the collimated beam and the flat side faces the focus spot. In our setup, we used plano-convex fused silica lenses.

The size of the laser focal spot on the sample can be estimated from:

$$\text{spot size} = D_{\text{dif}} + D_{\text{aber}} = \frac{4M^2 f}{\pi d} + \frac{nd^3}{f^2} \qquad (6)$$

where λ is laser excitation wavelength, *M* is the laser beam quality parameter (for the perfect fundamental transverse mode (TEM_{00}) mode, giving the perfect Gaussian beam, $M = 1$), *f* is the focusing lens focal length, *d* is the diameter of the incident beam, and *n* is the refractive index of the lens at wavelength λ. Figure 7 shows the calculated dependencies of the lens minimum focal spot size (cases A, B, and C for L_1; case D is considered for a large incident beam diameter for L_3, for example) dependence on the lens focal length for fixed laser beam diameters.

In the case of a narrow-beam diameter (*d*) of 1 mm, the focal spot size is determined primarily by the diffraction component (green line in Fig. 7A), except at very short focal lengths, < 2 cm. The focal spot size increases with the lens focal length and remains <40 μm for $f_{L_1} < 15$ cm. For a larger laser beam diameter, $d = 3$ mm, the focus spot size quickly increases as the lens focal length *f* becomes shorter than 5 cm due to the lens spherical aberrations (Fig. 7B). For $f > 8$ cm, the focal spot size is controlled by the diffraction component and slightly increases with lens focal length.

For a laser beam of $d = 5$ mm for focal lengths <15 cm, spherical aberrations dominate the spot size (blue curve, Fig. 7C). The focal spot size quickly increases for $f < 5$ cm, and becomes >100 μm for $f < 5$ cm. These data indicate that for laser beam diameters of 3–5 mm, the optimal focusing lens focal length is $f = 10$ to 15 cm. For larger laser beams, longer focal lengths are preferable due to the rapid increase in the contribution of spherical aberrations. Figure 7D shows the dependence of the focal spot size on the lens focal length for a lens similar to that used for L_3 that focuses light on the spectrometer entrance slit. In this case, the incident beam diameter of $d = 50$ mm results in large contribution of spherical aberrations. As the focal length decreases, the spherical aberration limited spot size increases and becomes >1000 μm for $f_{L_3} < 45$ cm (Fig. 7D).

The above analysis indicates that for a focusing lens L*3* of *f*-number, $f_{\#} < 9$, the spot on the spectrometer slit will be limited by spherical aberrations, and the spot size will be >1 mm. In this case, the spectrometer entrance slit must be >1 mm wide in order to transfer all of the collected light into the spectrometer independent of how small the laser beam spot size is on the sample.

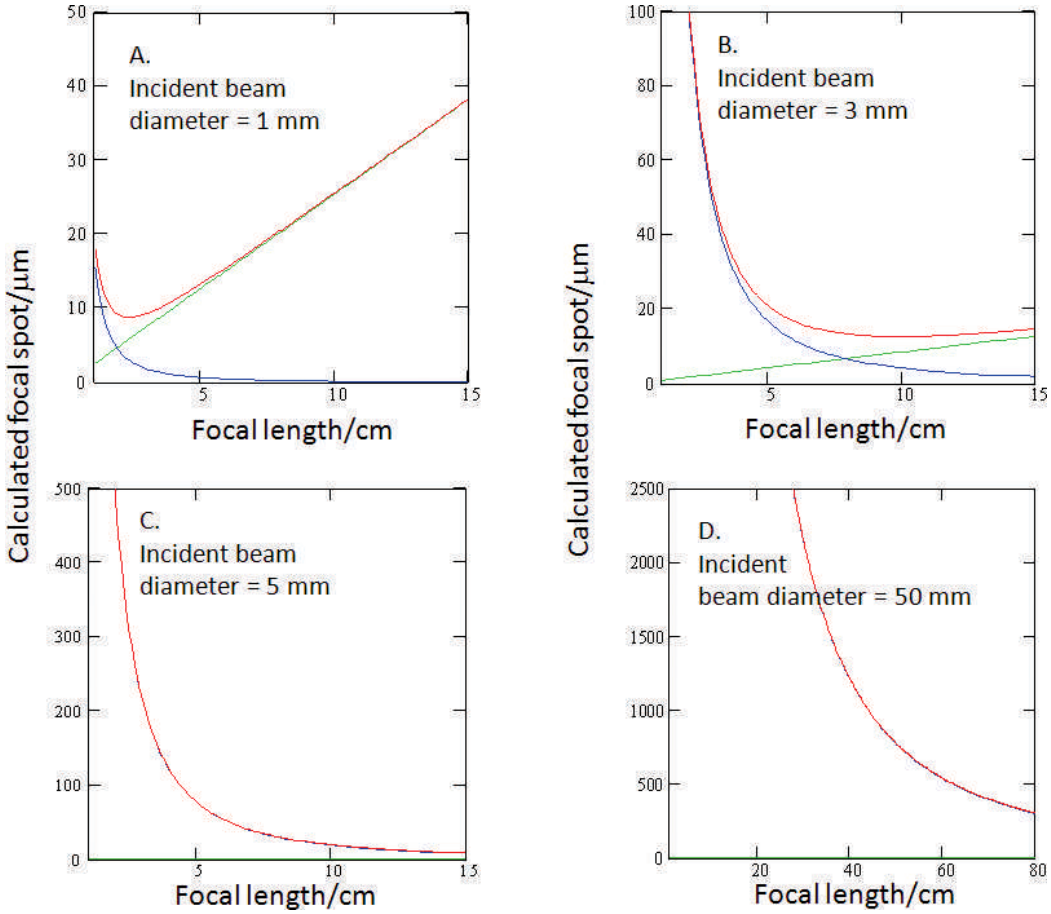

FIG. 7. Dependence of the spot size on the lens focal length for different incident beam diameters (d). The green curve is the diffraction component, the blue curve is the spherical aberration component, and the red curve is the sum that approximates focal spot size due to both diffraction and spherical aberrations. All calculations model a fused silica lens at $\lambda = 200$ nm, $n_{200\ nm} = 1.538$, and perfect TEM_{00} beam. (**A**) $d = 1$ mm. (**B**) $d = 3$ mm. (**C**) $d = 5$ mm. (**D**) $d = 50$ mm.

In general, lens L_3 is f-number matched to the spectrograph first collimating mirror. The f-number of our spectrometer is $f_{\#} = 12.5$. As L_3, we use a 5 cm diameter fused silica lens of $f_{L_3 at\ 580\ nm} = 75$ cm for the 589 nm Na D-line. At 200 nm, its focal length will be $f_{L_3 at\ 200\ nm}$ approximately 63 cm, giving an f-number $f_{\#L_3\ at\ 200\ nm} = 12.6$. This results in a spherical aberration limited spot size on the spectrometer slit of approximately 500 μm for a perfect Gaussian incident beam. If we operate our high-dispersion spectrometer with slit widths of 1 mm, the throughput will not be limited by the L_3 spherical aberrations, even if incident beam is not a perfect Gaussian.

Figure 6B estimates the maximum solid angle of scattered light, Ω_{max} that can be collected from a water–air interface. If Raman excitation occurs in a transparent liquid or solid, the scattered light must traverse the interface between the high refractive index sample and air. For the case of a water–air interface, 200 nm scattered light will be completely internally reflected for light at incidence angles greater than the critical angle $\Psi_c \approx 45°$. This allows a maximum light collection solid angle of $\Omega \approx 1.9$ steradians (sr) (Fig. 6B). An $f_{\#} = 0.5$ lens will accept this solid angle and will collect all scattered light that crosses the liquid–air interface. Our experimental observations indicate that utilizing L_2 with $f_{\#} < 1$ does not result in a significant spectrometer throughput increase, likely because of heavy spherical aberrations of such a collection lens.

SPECTROMETER PERFORMANCE

The Raman spectrometer performance was evaluated in the UV (229 nm) spectral regions. All spectra were recorded with a Roper Scientific liquid nitrogen–cooled PyLoN digital CCD detector, which has a 1340 × 400 array of 20 × 20 μm pixels.

Spectrograph Efficiency. Our spectrograph has total of six mirrors and two diffraction gratings. To determine the spectrograph efficiency, the UV reflectivity of all mirrors and gratings were experimentally measured at 229 nm. All six mirrors are coated with MgF_2-protected Al, and each has approximately 93% measured reflectivity at 229 nm. The holographic grating G_1 of the filter stage diffracts approximately 75% of the incident light in 1st order at 229 nm. The Echelle grating diffracts approximately 36% of the light into the 26th order at 229 nm. The overall efficiency of our spectrograph (four off-axis parabolic mirrors, two plane mirrors, and two gratings) at 229 nm is calculated to be approximately 18%.

Spectrometer Throughput and Resolution. We compared the performance of our Echelle spectrograph with a SPEX Triplemate 1877B spectrometer[26] that is optimized for 229 nm in our laboratory. The Triplemate spectrometer utilizes dielectric stack mirror coatings optimized for the UV region, two 600 grooves/mm gratings blazed at 500 nm in the first order (or for 250 nm in the second order) for the filter stage, and 1200 grooves/mm grating blazed for 500 nm in the first

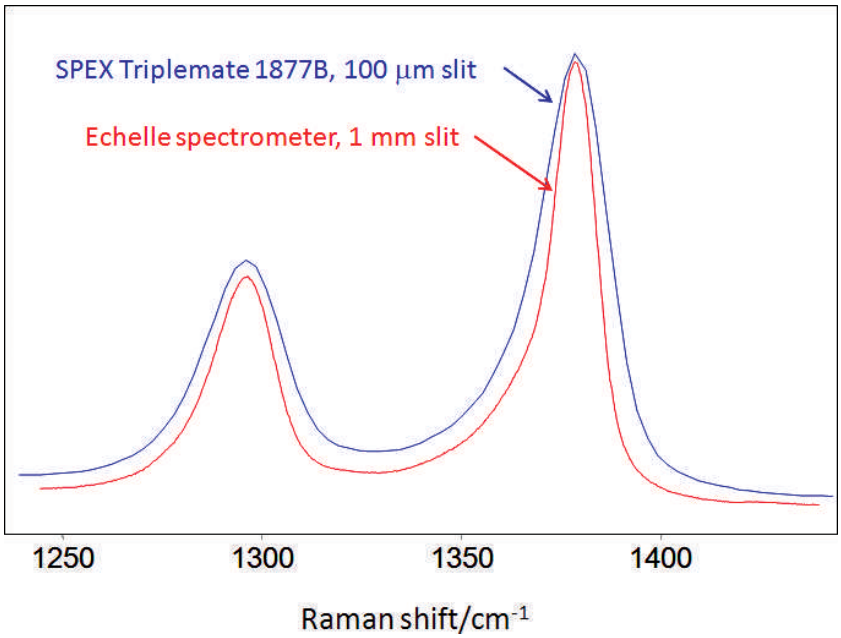

FIG. 8. Overlapped 229 nm Raman spectra of Teflon obtained with the SPEX Triplemate 1877B (slit width = 100 μm) and our Echelle spectrograph (slit width = 1 mm).

order (or for 250 nm in the second order). The overall measured efficiency of the Triplemate was approximately 3%.[26] Figure 8 shows the Raman spectra of Teflon in the 1250–1450 cm^{-1} region.

Our Echelle spectrograph used with a 1 mm entrance slit width provides better resolution than the Triplemate used with an entrance slit width of 100 μm, using the same detector and excitation wavelength and power. The FWHM of the measured Teflon band at 1375 cm^{-1} obtained with our Echelle spectrometer is approximately 11 cm^{-1}, while for the Triplemate, it is approximately 17 cm^{-1}.

Figure 9 shows the same region of the Teflon Raman spectra measured with the same detector, accumulation time, excitation wavelength, and power for the Triplemate and Echelle spectrographs. The integrated area of the band at approximately 1295 cm^{-1} that we used to monitor the spectrograph throughputs is approximately 35× larger for the Echelle spectrograph, with a 1 mm slit compared with that of the SPEX Triplemate with 100 μm slit. In spite of the 1 mm slit, our Echelle spectrograph provides better resolution than does the SPEX Triplemate using a 100 μm slit (Fig. 8).

Figures 10A–10C show the dependence of the measured bandwidth of the Echelle spectrograph on the entrance slit width. The limiting resolution is approximately four CCD pixels, which corresponds to approximately 0.6 cm^{-1} at 229

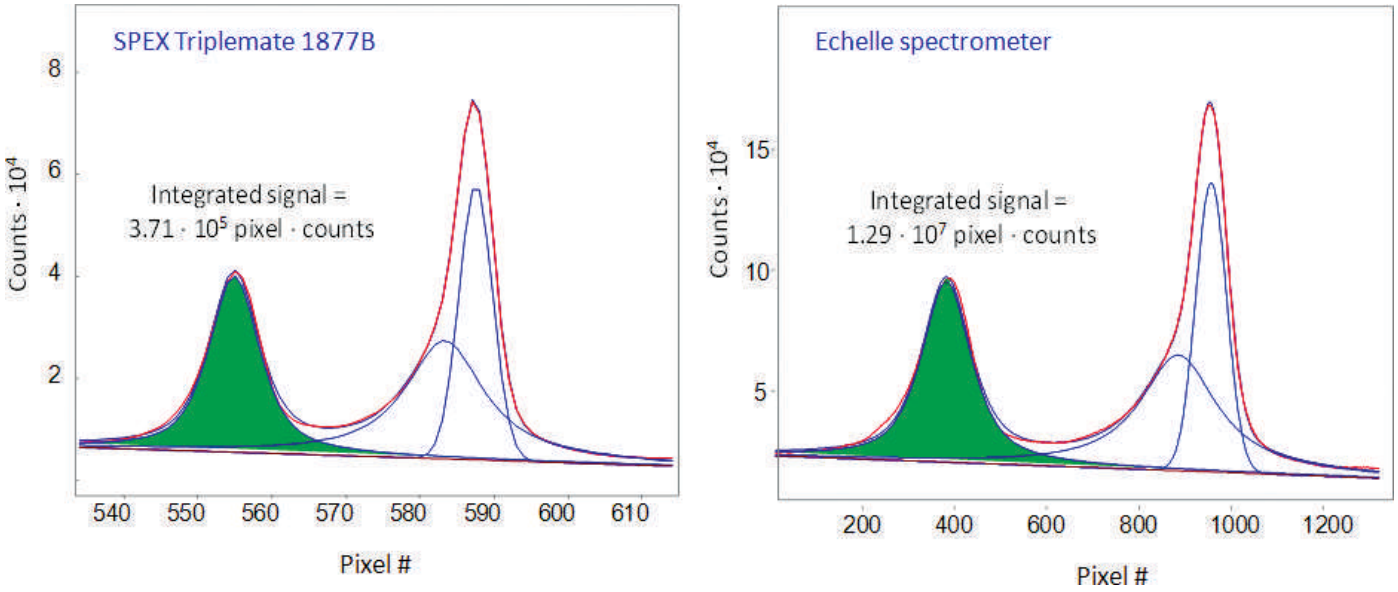

FIG. 9. Spectral fit of the 229 nm Raman spectra of Teflon obtained with the SPEX Triplemate (slit width = 100 μm) and our Echelle spectrograph (slit width = 1 mm).

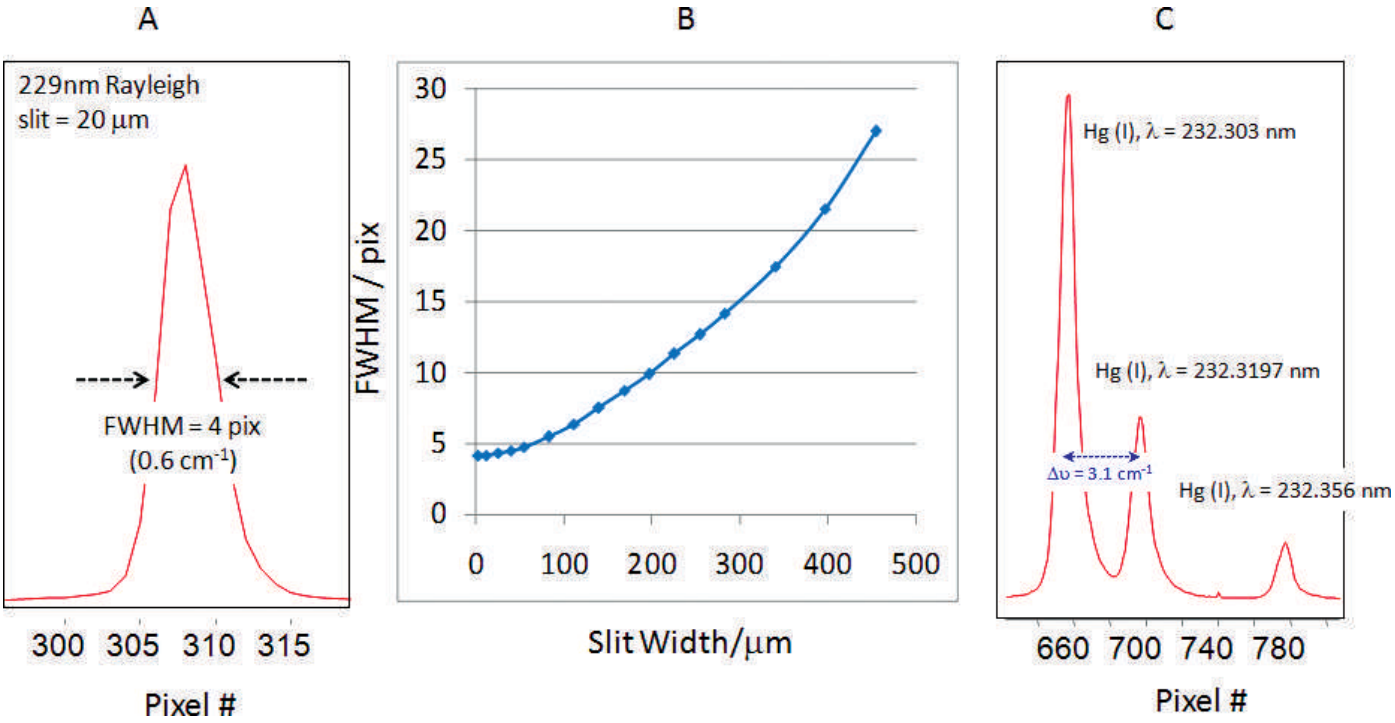

FIG. 10. Echelle spectrometer resolution. (**A**) Spectrum of 229 nm laser Rayleigh scattering from Teflon. At a slit width = 20 µm, the resolution is about 4 pixels, which is approximately 0.6 cm^{-1}. (**B**) Slit width dependence of the FWHM of the 229 nm Rayleigh line scattered from the Teflon. (**C**) Atomic spectrum of the mercury, an Hg(I) triplet at 232 nm. Wavelengths of the mercury lines are taken from the National Institute of Science and Technology Atomic Spectra Database.

nm. The Hg(I) atomic spectrum 232 nm triplet of closely spaced lines is completely resolved.

Spectrometer Transfer Function at Entrance Slit = 1 mm. The wide entrance slit dramatically increases spectrometer throughput, but it also affects the observed Raman spectral band shapes. The 1 mm wide slit creates an approximately 1 mm wide image on the CCD detector, which is about 50 pixels. Figure 11 shows the band shape created by Echelle spectrometer if monochromatic light (204 nm Rayleigh line scattered from the Teflon surface) is focused through a 1 mm opened slit to form a CCD image.

Reciprocal Linear Dispersion: 229 nm UV Raman of Inorganic Salts. Figure 12 shows the Raman spectrum of solid Na_2SO_4, measured by our Echelle spectrometer. At 229 nm excitation the 1 in (2.54 cm) CCD accommodates approximately 200 cm^{-1} of the Raman spectrum showing RLD_{229} = 0.147 cm^{-1} per pixel = 0.04 nm/mm. The FWHM of the SO_4^{2-} band is about 5 cm^{-1}.

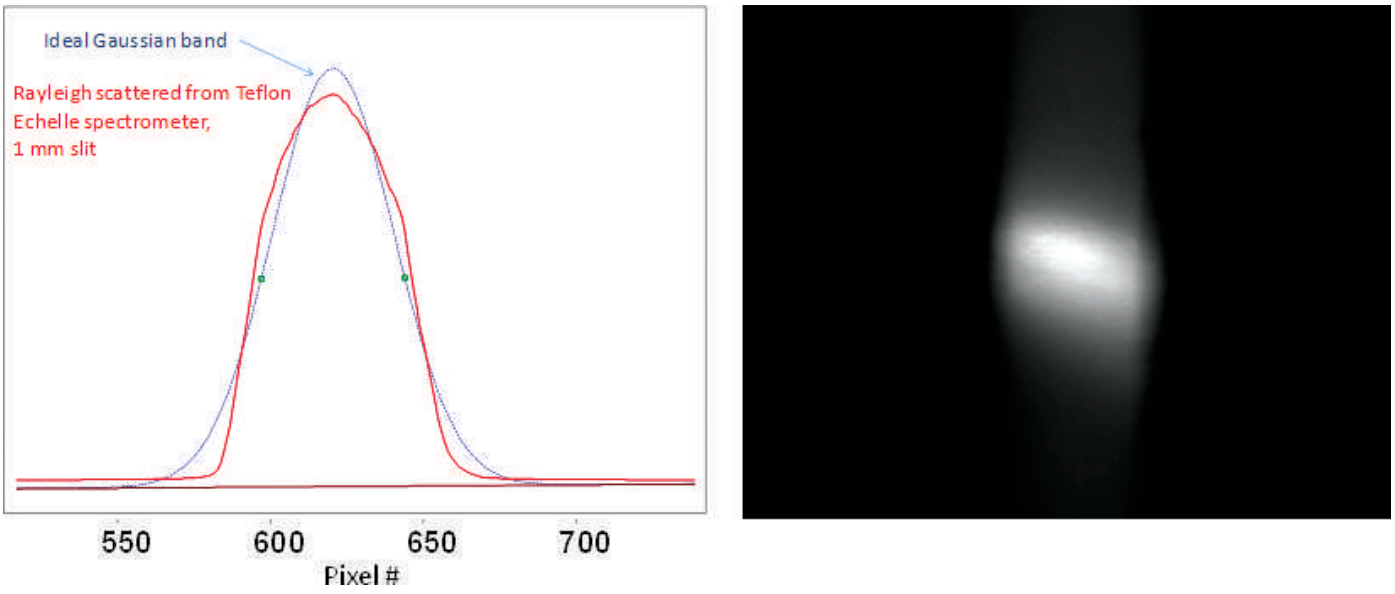

FIG. 11. Band shape of monochromatic light (laser Rayleigh scattered from Teflon) focused onto 1 mm slit (red) compared with Gaussian band shape. Image of 1 mm slit on a CCD.

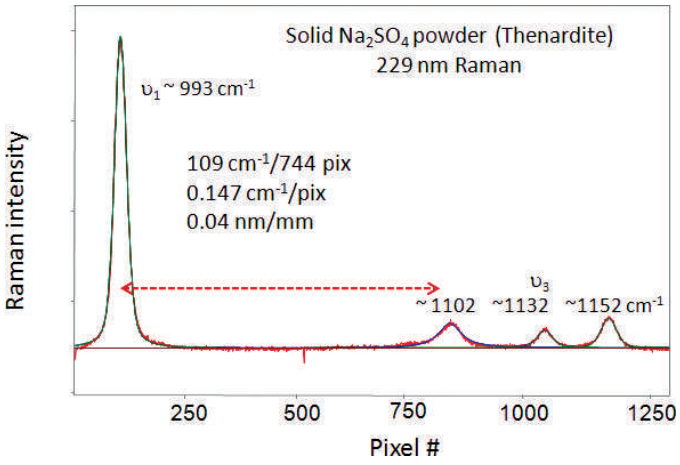

FIG. 12. Raman spectra of solid Na_2SO_4 powder (thenardite phase), measured with high-resolution, high-dispersion Echelle Raman spectrograph.

Echelle Spectrometer Free Spectral Range. Figure 13 compares the UV resonance Raman spectra of Gly_2 in water, measured by our subtractive dispersion double monochromator spectrograph[25] (top), with that of our high-resolution and high-throughput Echelle spectrograph (bottom). The CCD-limited free spectral range of the Echelle spectrometer is about eight times smaller, $FSR_{Echelle,\ 229\ nm}$ approximately 200 cm^{-1}.

Ability to Resolve 1% Change in the UV Resonance Raman Spectroscopy Spectrum of Peptide. UV resonance Raman spectroscopy (UVRR) is very useful for investigating protein–protein, protein–drug interactions, and other biological events that involve small changes in protein structure. We experimentally determined the ability of our spectrograph to detect small changes in the peptide bond spectra.

Figure 14 shows two overlapping UVRR spectra of a 20 mg/ml aqueous solution of Gly_2 (green) and the same solution but with 0.2 mg/ml of Ala_2 added (red, 1 mass% or 0.84 molar% of peptide bonds) and their difference spectrum. The difference spectrum clearly shows the UVRR spectrum of the 1% added Ala_2. The $C_\alpha H$ band of the Ala_2 at approximately 1410 cm^{-1} is clearly differentiable, since it is up-shifted compared with the $C_\alpha H_2$ bending band of Gly_2 at 1390 cm^{-1}, for example. The amide III band of Ala_2 appears up-shifted by approximately 5 cm^{-1} compared with that of pure Ala_2. This appears to result from small spectral shifts of the spectrograph in response to small changes in the temperature. We are working to thermally stabilize our spectrograph to avoid these shifts.

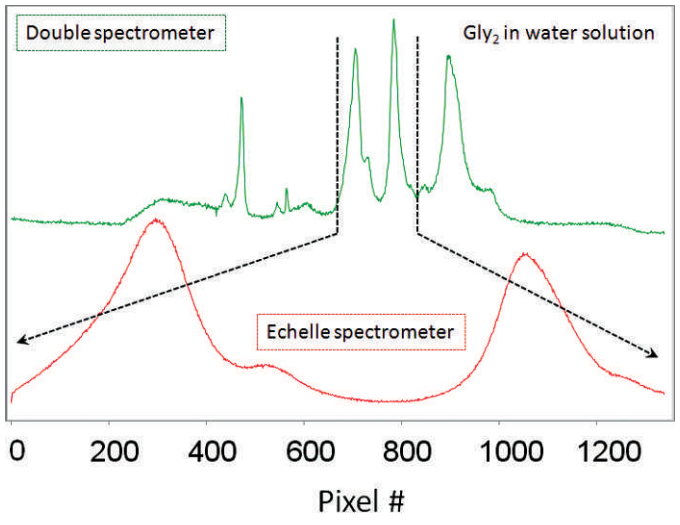

FIG. 13. Free spectral range, double subtractive spectrometer[24] vs. Echelle spectrometer. Spectra of Gly_2 in water obtained with our double-subtractive spectrograph (204 nm excitation in resonance with peptide bond $\pi \rightarrow \pi^*$ transition, 100 μm slit) compared with that measured with our high-throughput, high-resolution Echelle spectrograph (229 nm pre-resonance Raman, 1 mm slit).

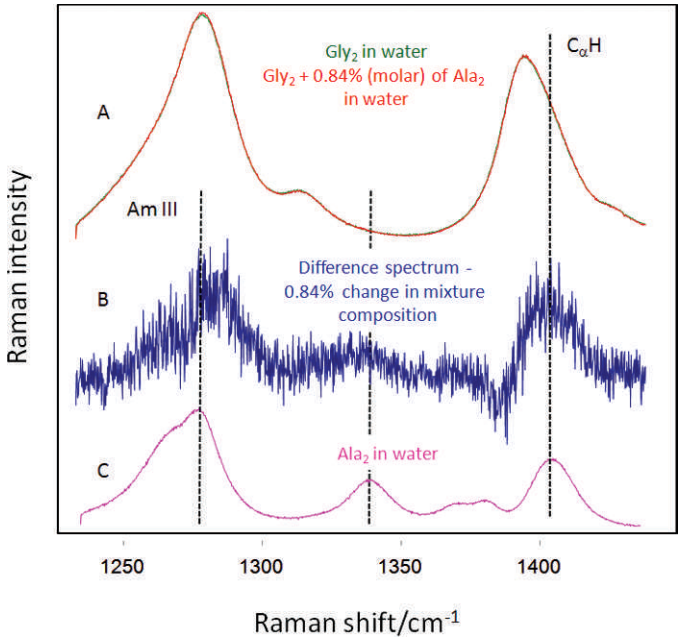

FIG. 14. (**A**) 229 nm UVRR spectra of 20 mg/ml Gly_2 aqueous solution (green) and 20 mg/ml aqueous solution of Gly_2 + 0.2 mg/ml of Ala_2 (red). (**B**) Magnified difference spectrum. (**C**) UVRR spectrum of 20 mg/ml aqueous solution of Ala_2. Spectra obtained with our Echelle spectrograph, 15 min accumulation times.

CONCLUSION

We designed and fabricated a novel UV Raman high-throughput and high-dispersion spectrograph that dramatically increases the sensitivity of UV Raman spectroscopy. The experimentally determined limiting spectral resolution at minimal slit width at 229 nm is about 0.6 cm^{-1}. The reciprocal linear dispersion of our Echelle spectrometer is about 0.04 nm/mm at 229 nm. This high dispersion allowed us to open entrance slit to 1 mm while maintaining a spectral resolution of approximately 10 cm^{-1} FWHM, close to that of the homogeneous line widths of biological macromolecules. The spectrograph design utilizes a high dispersion Echelle grating in light-efficient out-of-plane optical configuration. The throughput of this spectrograph is 35× times that of our previously optimized UV Raman spectrographs. We demonstrate the ability of this spectrograph to easily measure UVRR spectra of peptides with S/N high enough to easily monitor <1% changes in peptide composition at less than 15 min accumulation times.

ACKNOWLEDGMENTS

This work was supported by NIH 1R01EB009089 and ONR N00014-12-1-0021 grants.

1. S.A. Oladepo, K. Xiong, Z. Hong, S.A. Asher, J. Handen, I.K. Lednev. "UV Resonance Raman Investigations of Peptide and Protein Structure and Dynamics". Chem. Rev. 2012. 112(5): 2604-2628.
2. G. Balakrishnan, Y. Hu, T. G. Spiro, "His26 Protonation in Cytochrome c Triggers Microsecond β-Sheet Formation and Heme Exposure: Implications for Apoptosis". J. Am. Chem. Soc. 2012. 134(46): 19061-19069.
3. S. Niebling, H.Y. Kuchelmeister, C. Schmuck, S. Schluecker. "Quantitative Label-Free Monitoring of Peptide Recognition by Artificial Receptors: A Comparative FT-IR and UV Resonance Raman Spectroscopic Study". Chem. Sci. 2012. 3(12): 3371-3377.
4. C.M. Halsey, O.O. Oshokoya, R.D. Jiji, J.W. Cooley. "Deep-UV Resonance Raman Analysis of the *Rhodobacter capsulatus* cytochrome bc_1 Complex Reveals a Potential Marker for the Transmembrane Peptide Backbone". Biochemistry. 2011. 50(30): 6531-6538.
5. S. Nagatomo, M. Nagai, T. Kitagawa. "A New Way to Understand Quaternary Structure Changes of Hemoglobin upon Ligand Binding on the Basis of UV-Resonance Raman Evaluation of Intersubunit Interactions". J. Am. Chem. Soc. 2011. 133(26): 10101-10110.
6. I.K. Lednev, V. Shashilov, M. Xu. "Ultraviolet Raman Spectroscopy is Uniquely Suitable for Studying Amyloid Diseases". Curr. Sci. 2009. 97(2): 180-185.
7. J.M. Benevides, S.A. Overman, G.J. Thomas, Jr. "Raman, Polarized Raman, and Ultraviolet Resonance Raman Spectroscopy of Nucleic Acids and Their Complexes". J. Raman Spectrosc. 2005. 36(4): 279-299.
8. I.K. Lednev, A.S. Karnoup, M.C. Sparrow, S.A. Asher. "α-Helix Peptide Folding and Unfolding Activation Barriers: A Nanosecond UV Resonance Raman Study". J. Am. Chem. Soc. 1999. 121(35): 8074-8086.
9. I.K. Lednev, A.S. Karnoup, M.C. Sparrow, S.A. Asher. "Transient UV Raman Spectroscopy Finds No Crossing Barrier Between the Peptide α-Helix and Fully Random Coil Conformation". J. Am. Chem. Soc. 2001. 123(10): 2388-2392.
10. T. Kitagawa, N. Haruta, Y. Mizutani. "Time-Resolved Resonance Raman Study on Ultrafast Structural Relaxation and Vibrational Cooling of Photodissociated Carbonmonoxy Myoglobin". Biopolymers. 2002. 61(3): 207-213.
11. C.-Y. Huang, G. Balakrishnan, T.G. Spiro. "Early Events in Apomyoglobin Unfolding Probed by Laser T-Jump–UV Resonance Raman Spectroscopy". Biochemistry. 2005. 44(48): 15734-15742.
12. A.V. Mikhonin, S.A. Asher, S.V. Bykov, A. Murza. "UV Raman Spatially Resolved Melting Dynamics of Isotopically Labeled Polyalanyl Peptide: Slow A-Helix Melting Follows 310-Helices and π-Bulges Premelting". J. Phys. Chem. B. 2007. 111(12): 3280-3292.
13. G. Balakrishnan, C.L. Weeks, M. Ibrahim, A.V. Soldatova, T.G. Spiro. "Protein Dynamics from Time-Resolved UV Raman Spectroscopy". Curr. Opin. Structr. Biol. 2008. 18(5): 623-629.
14. S.F. El-Mashtoly, M. Kubo, S. Nakashima, T. Shimizu, T. Kitagawa. "Structural Dynamics of EcDOS Heme Domain Revealed by Time-Resolved Ultraviolet Resonance Raman Spectroscopy". J. Phys. Chem. Lett. 2011. 2(17): 2212-2217.
15. S.A. Oladepo, K. Xiong, Z. Hong, S.A. Asher. "Elucidating Peptide and Protein Structure and Dynamics: UV Resonance Raman Spectroscopy". J. Phys. Chem. Lett. 2011. 2(4): 334-344.
16. S.A. Asher, A.V. Mikhonin, S. Bykov. "UV Raman Demonstrates that α-Helical Polyalanine Peptides Melt to Polyproline II Conformations". J. Am. Chem. Soc. 2004. 126(27): 8433-8440.
17. D.J. Schroeder, R.L. Hilliard. "Echelle Efficiencies: Theory and Experiment". Appl. Opt. 1980. 19(16): 2833-2841.
18. M.J. Pelletier. "Raman Spectroscopy Using an Echelle Spectrograph with CCD Detection". Appl. Spectrosc. 1990. 44(10): 1699-1705.
19. M.R. Torr, D.G. Torr. "Imaging Spectrometer for High-Resolution Measurements of Stratospheric Trace Constituents in the Ultraviolet". Appl. Opt. 1988. 27(3): 619-626.
20. M.A. Gil, J.M. Simon. "Aberrations in Off-Plane Spectrometers". Opt. Acta. 1983. 30(9): 1287-1301.
21. P. Lindblom. "Theory of the Two-Mirror Plane-Grating Spectrograph". J. Opt. Soc. Am. 1972. 62(6): 756-762.
22. J.J. Mitteldorf, D.O. Landon. "Multiply Diffracted Light in the Czerny–Turner Spectrometer". Appl. Opt. 1968. 7(8): 1431-1435.
23. C.M. Penchina. "Reduction of Stray Light in In-Plane Grating Spectrometers". Appl. Opt. 1967. 6(6): 1029-1031.
24. J.K. Pribram, C.M. Penchina. "Stray Light in Czerny–Turner and Ebert Spectrometers". Appl. Opt. 1968. 7(10): 2005-2014.
25. S. Bykov, I. Lednev, A. Ianoul, A. Mikhonin, C. Munro, S.A. Asher. "Steady-State and Transient Ultraviolet Resonance Raman Spectrometer for the 193–270 nm Spectral Region". Appl. Spectr. 2005. 59(12): 1541-1552.
26. S.A. Asher, C.R. Johnson, J. Murtaugh. "Development of a New UV Resonance Raman Spectrometer for the 217–400-nm Spectral Region". Rev. Sci. Instrum. 1983. 54(12): 1657-1662.